Supporting Information

Self-Assembly Magnetized 3D Hierarchical Graphite Carbon-Based Heterogeneous Yolk-Shell Nanoboxes with Enhanced Microwave Absorption

Wenjun Ma,[a] Peng He,[a] Jian Xu,[a] Xiaoyun Liu,[a] Shaoliang Lin,*[a] Zhong-Kai Cui,[b] Peiyuan Zuo[a] and Qixin Zhuang*[a]

[a] *Key Laboratory of Advanced Polymer Materials of Shanghai, School of Material Science and Engineering, East China University of Science and Technology, Shanghai 200237, P. R. China*

[b] *School of Basic Medical Sciences, Southern Medical University, Guangzhou 510515, P. R. China*

*Corresponding author.

Email address: slin@ecust.edu.cn (S. Lin), qxzhuang@ecust.edu.cn (Q. Zhuang).

Experimental Section

Materials

Potassium ferricyanide ($K_3[Fe(CN)_6]$), trisodium citrate dihydrate, cobalt nitrate hexahydrate ($Co(NO_3)_2{\cdot}6H_2O$), tetraethyl orthosilicate (TEOS), resorcinol, formaldehyde (37 wt%), concentrated ammonia solution ($NH_3{\cdot}H_2O$, 25~28 wt%) and absolute ethanol (EtOH) were of analytical grade (Shanghai Titan Technology Co., Ltd.). Deionized (DI) water was used for all experiments. All chemicals were used without any further purification.

Synthesis of FeCo PBA nanocubes

In a typical synthesis procedure, 1.75 g of $Co(NO_3)_2{\cdot}6H_2O$ and 2.65 g of trisodium citrate dihydrate were dissolved in 200 mL of DI water to form solution A. 1.32 g $K_3[Fe(CN)_6]$ was dissolved in 200 mL of DI water to form solution B. After that, solution B was added into solution A and stirred continuously for about 1 min. Then the obtained mixed solution was aged

at room temperature for 24 h. The precipitate was collected by centrifugation, then washed with DI water and EtOH several times and dried overnight at 60 ℃.

Synthesis of FeCo PBA@SiO_2 nanocubes

0.07 g FeCo PBA nanocubes were ultrasonically dispersed in a mixture of 50 mL DI water and 200 mL EtOH, followed by the addition of 3 mL $NH_3 \cdot H_2O$ to create an alkaline environment. Then 2 mL TEOS was added into the suspension under magnetic stirring for ~20 min. After reacting at room temperature for 4 h, the product was washed with DI water and EtOH several times and dried overnight at 60 ℃ to yield FeCo PBA@SiO_2 nanocubes.

Synthesis of FeCo PBA@SiO_2@PR nanocubes

0.07 g FeCo PBA@SiO_2 nanocubes were dispersed in a mixture of 100 mL DI water, 200 mL EtOH and 6 mL $NH_3 \cdot H_2O$. Then 0.7 g resorcinol and 0.98 mL formaldehyde were added into the suspension successively under magnetic stirring. 10 h later, the product was washed several times and dried overnight at 60 ℃ to obtain FeCo PBA@SiO_2@PR nanocubes.

Synthesis of FeCo/GC@SiO_2@C nanocubes

FeCo PBA@SiO_2@PR nanocubes were carbonized in a tubular furnace at 650 ℃ for 6 h (heating rate: 5 ℃ min^{-1}) under N_2 atmosphere, and then FeCo/GC@SiO_2@C nanocubes were obtained.

Synthesis of YS-FCF/GC@C nanoboxes

Furthermore, FeCo/GC@SiO_2@C nanocubes were ultrasonically dispersed in 80 mL DI water at room temperature, and then the homogeneous suspension was transferred to a stainless-steel autoclave lined with Teflon. The mixture was heated at 200 ℃ for 15 h and then naturally cooled to room temperature. The product was washed several times with DI water and EtOH and then dried at 60 °C for 12 h. The obtained product was noted as YS-FCF/GC@C, for during the hydrothermal process, FeCo experienced a succession of redox reactions and transformed into a combination of FoCo, $CoFe_2O_4$, and $Fe(OH)_3$.

Synthesis of FCF/GC nanocubes

FeCo PBA@SiO_2 nanocubes were carbonized in a tubular furnace at 650 ℃ for 6 h (heating rate: 5 ℃ min^{-1}) under N_2 atmosphere, thereby FeCo/GC@SiO_2 nanocubes were obtained.

Furthermore, FeCo/GC@SiO_2 nanocubes were ultrasonically dispersed in 80 mL DI water at room temperature, and then the homogeneous suspension was transferred to a stainless-steel

autoclave lined with Teflon. The mixture was heated at 200 ℃ for 15 h and next naturally cooled to room temperature. The product was washed several times with DI water and EtOH, then dried at 60 °C for 12 h. The obtained product was noted as FCF/GC.

Synthesis of FCF/GC@C-1 nanocubes

0.03 g FeCo PBA nanocubes were dispersed in a mixture of 50 mL DI water, 100 mL EtOH and 3 mL $NH_3 \cdot H_2O$. Then 0.3 g resorcinol and 0.42 mL formaldehyde were added into the suspension successively under magnetic stirring. 10 h later, the product was washed several times and dried overnight at 60 ℃ to obtain FeCo PBA@PR nanocubes.

FeCo PBA@PR nanocubes were carbonized in a tubular furnace at 650 ℃ for 6 h (heating rate: 5 ℃ min^{-1}) under N_2 atmosphere, and then FeCo/GC@C nanocubes were obtained. Furthermore, FeCo/GC@C nanocubes were ultrasonically dispersed in 80 mL DI water at room temperature, and next the homogeneous suspension was transferred to a stainless-steel autoclave lined with Teflon. The mixture was heated at 200 ℃ for 15 h, followed by natural cooling to room temperature. The product was washed several times with DI water and EtOH and then dried at 60 °C for 12 h. The obtained product was noted as FCF/GC@C-1.

Synthesis of YS-FeCo/GC@C-KOH nanocubes

0.05 g FeCo/GC@SiO_2@C nanocubes and 0.2 mol KOH were ultrasonically dispersed in 60 mL DI water. The mixture was kept at 60 °C under mechanical agitation for15 h and followed by washing several times with DI water and EtOH, and dried at 60 °C for 12 h. The obtained product was noted as YS-FeCo/GC@C-KOH.

Synthesis of FCF/GC-1 nanocubes

FeCo PBA nanocubes were carbonized in a tubular furnace at 650 ℃ for 6 h (heating rate: 5 ℃ min^{-1}) under N_2 atmosphere, and thereby FeCo/GC nanocubes were obtained.

Furthermore, FeCo/GC nanocubes were ultrasonically dispersed in 80 mL DI water at room temperature, and then the homogeneous suspension was transferred to a stainless-steel autoclave lined with Teflon. The mixture was heated at 200 ℃ for 15 h and then naturally cooled to room temperature. The product was washed several times with DI water and EtOH, then dried at 60 °C for 12 h. The obtained product was noted as FCF/GC-1.

Materials Characterization

GeminiSEM 500 was employed to obtain scanning electron microscope (SEM) images and

energy dispersive spectroscopy (EDS) images. Transmission electron microscope (TEM) images and high-resolution transmission electron microscope (HRTEM) images were obtained using a JEOL JEM-2100 with an acceleration voltage of 200 kV. X-ray photoelectron spectroscopy (XPS, ESCALAB 250Xi) spectra were collected using Al Kα radiation. Fourier transform infrared spectroscopy (FT-IR) spectra were acquired using a Nicolet is50 spectrometer. The compositions and crystal characteristics of samples were measured by X-ray diffraction (XRD, D/max 2550VB/PC, 2θ=10°-80°) under the radiation of Cu Kα. Raman spectra were acquired on a laser micro-Raman spectrometer (≤ 10.2/cm/invia reflex) assembling with a 532 nm laser. The magnetic properties were identified using a vibrating sample magnetometer (VSM, Quantum Design PPMS DynaCool, LakeShore 7404). The N_2 adsorption-desorption isotherms, specific surface area and pore size distribution were described by the Brunauer-Emmett-Teller (BET) method *via* a TriStar II 3flex analyzer. A vector network analyzer (Agilent, PNA-N5244A) was used to determine electromagnetic parameters by the coaxial method. The absorber was uniformly immersed in the molten paraffin at a mass fraction of 40%, followed by modeling into a ring-shaped sample with an outer diameter of 7.0 mm and an inner diameter of 3.04 mm for further tests.

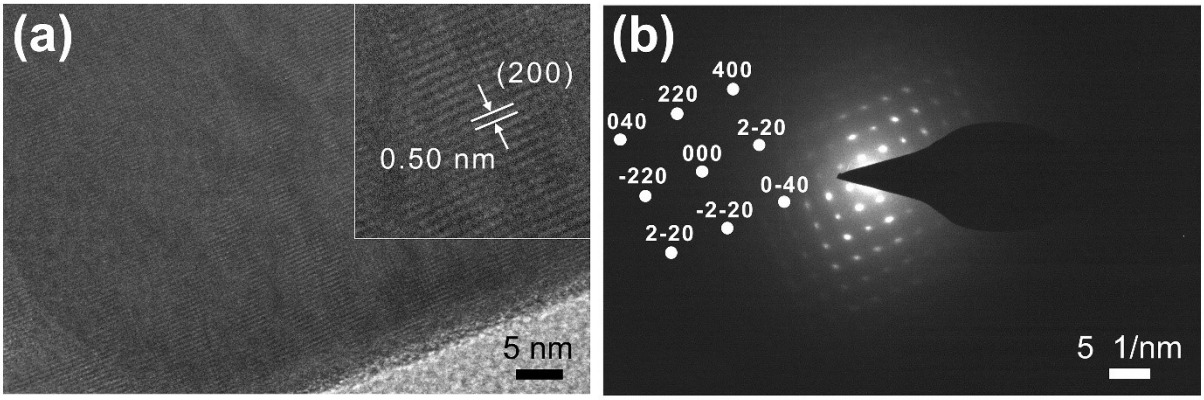

Fig. S1. (a) HRTEM image and (b) SAED pattern of FeCo PBA.

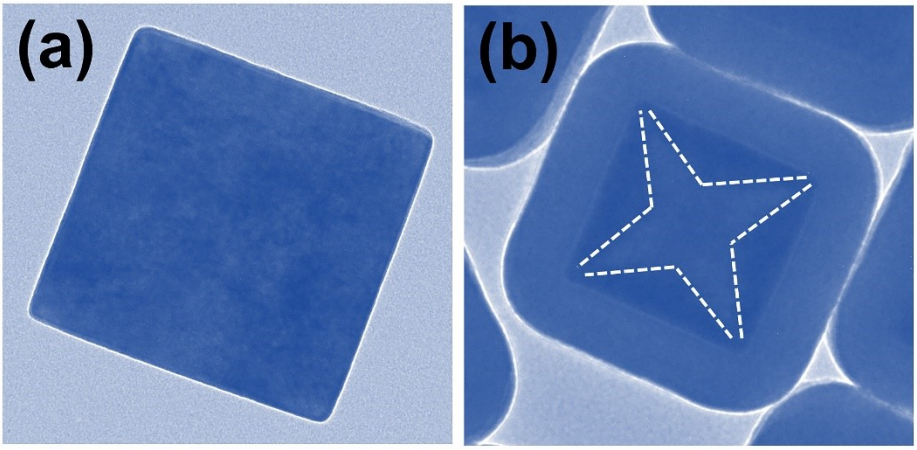

Fig. S2. TEM images of (a) FeCo PBA and (b) FeCo PBA@SiO_2 dyed with blue.

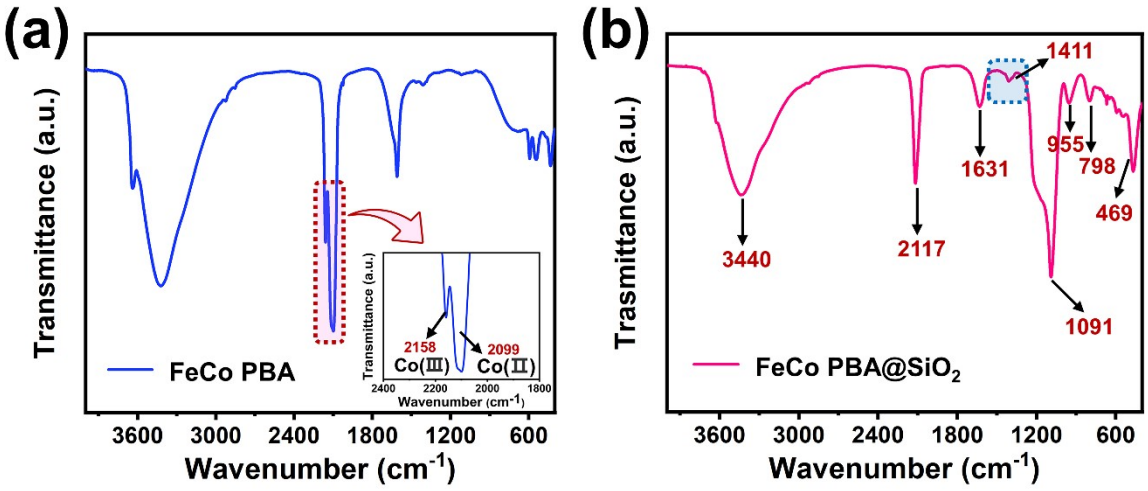

Fig. S3. FT-IR spectra of (a) FeCo PBA and (b) FeCo PBA@SiO_2.

The cube-to-cage transformation was due to the different reactivity of corners and plane surfaces of FeCo PBA nanocubes on account of different compositions.[1, 2] $NH_3 \cdot H_2O$ worked as a cavity creator by means of site-selective chemical etching. As a matter of fact, Fe^{II}-C-N-Co^{III} and Fe^{II}-C-N-Co^{II} species coexisted in the nanocubes with the inhomogeneous distribution. Fe^{II}-C-N-Co^{III} species were mainly distributed at the center and corners, while Fe^{II}-C-N-Co^{II} species were located near the surfaces.[1] During the etching process, unstable Fe^{II}-C-N-Co^{III} species ruptured, resulting in a diffusive etching inside the FeCo PBA. The instability of Co^{III} bonding and the occurrence of the etching process could be observed in FI-IR spectra (Fig. S3a), in which FeCo PBA exhibited two peaks situated at 2158 cm^{-1} and 2099 cm^{-1} representing Co^{III} and Co^{II}, respectively.[3] The following reaction (Equation (1)) was probably involved during the etching process:[4]

$$6[Co(CN)_6]^{3-}+8NH_3 \rightarrow 6[Co(CN)_6]^{4-}+N_2\uparrow+6NH_4^+ \quad (1)$$

A ν (NH) peak representing NH^{4+} at 1411 cm^{-1} in the FT-IR spectra (Fig. S3b) emerged at the later stage of the SiO_2 coating process, indicating the etching effect of $NH_3 \cdot H_2O$, and also the peak of Co^{III} disappeared, which implied all Co^{III} was converted to Co^{II} according to the aforementioned reaction. Accordingly, the net result was that the formation of the cavity was accomplished.

Moreover, for FeCo PBA@SiO_2 nanocubes, the characteristic peaks at 798 cm^{-1} and 1091 cm^{-1} could be attributed to the symmetrical and antisymmetric stretching vibration of Si-O-Si, respectively. The characteristic peak at 469 cm^{-1} was associated with Si-O bending vibration and the peak at 955 cm^{-1} was due to the bending vibration of Si-OH.[5] And two characteristic

peaks located at 3440 cm^{-1} and 1631 cm^{-1} corresponded to the stretching vibration and bending vibration of -OH in absorbed water, respectively.

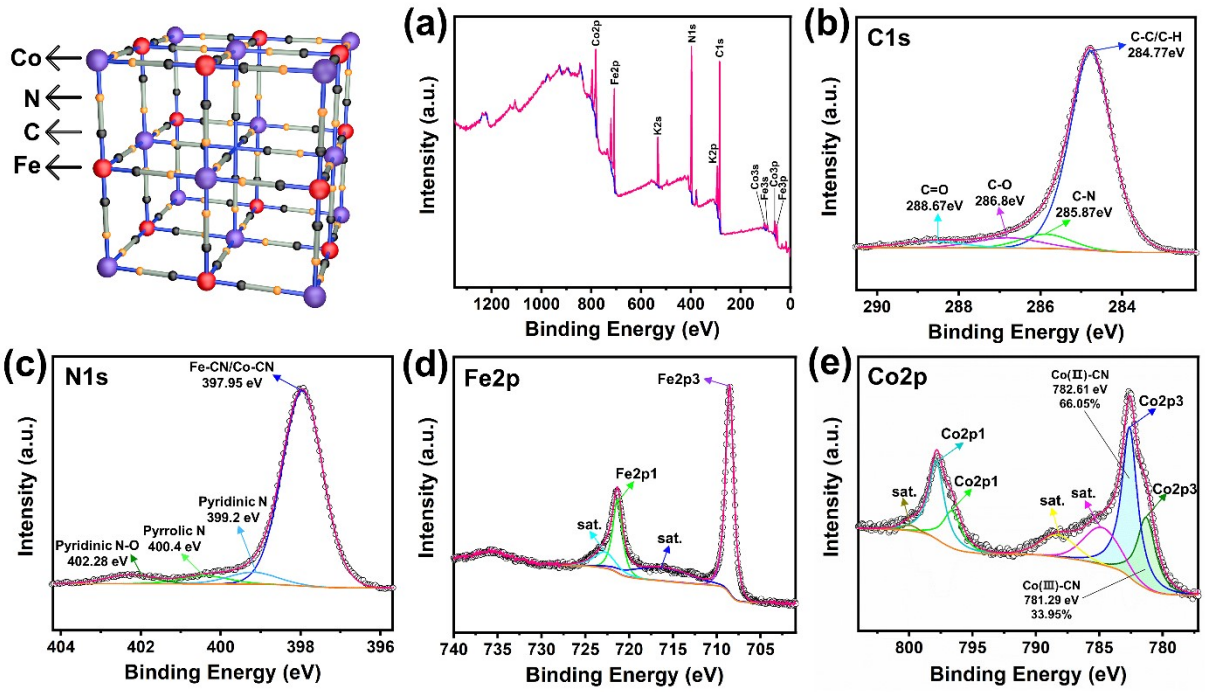

Fig. S4. XPS spectra of FeCo PBA.

There were two valence states of Co element in FeCo PBA (Fig. S4e), the proportion of Co^{II}-CN was 66.05%, which was more abundant than the 33.95% for Co^{III}-CN. The N 1s spectrum was deconvoluted into four characteristic peaks, corresponding to pyridinic N-O (402.28 eV), pyrrolic N (400.4 eV), pyridinic N (399.2 eV) and Fe-CN/Co-CN (397.95 eV), respectively.[6, 7]

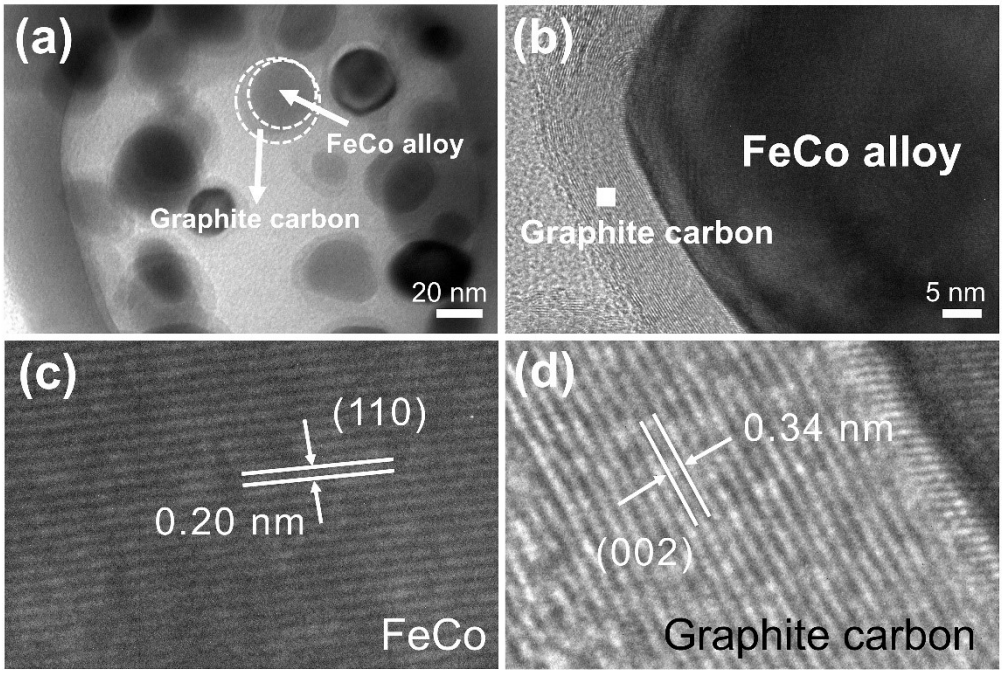

Fig. S5. HRTEM images of FeCo/GC@SiO_2@C.

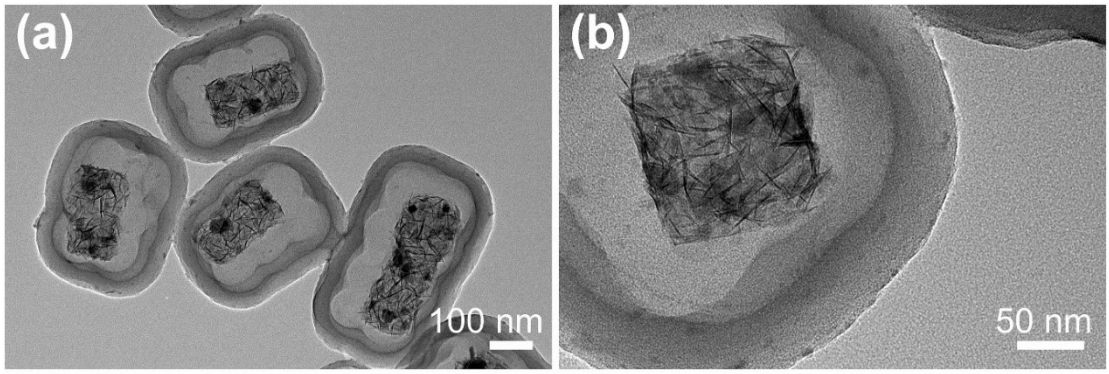

Fig. S6. TEM images of NiFe PBA-based nanoboxes obtained from hydrothermal process.

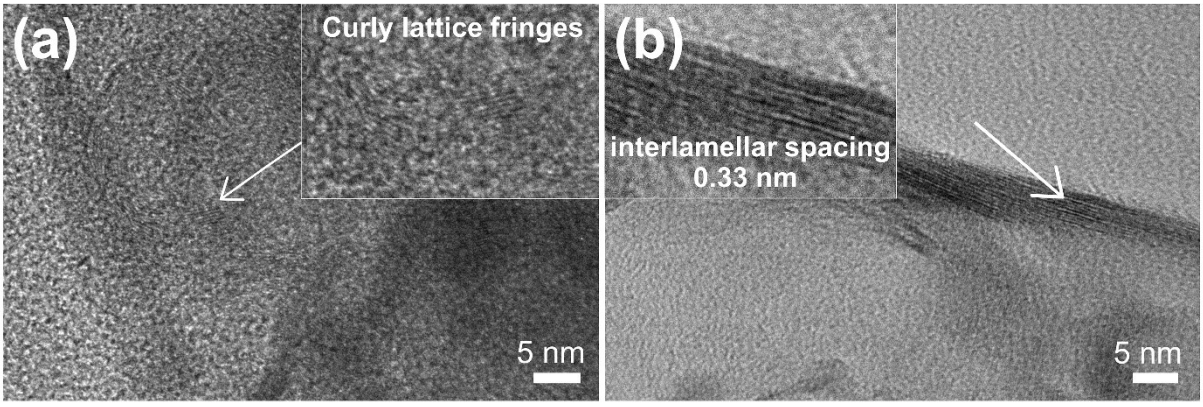

Fig. S7. HRTEM images of lamellar GC**.**

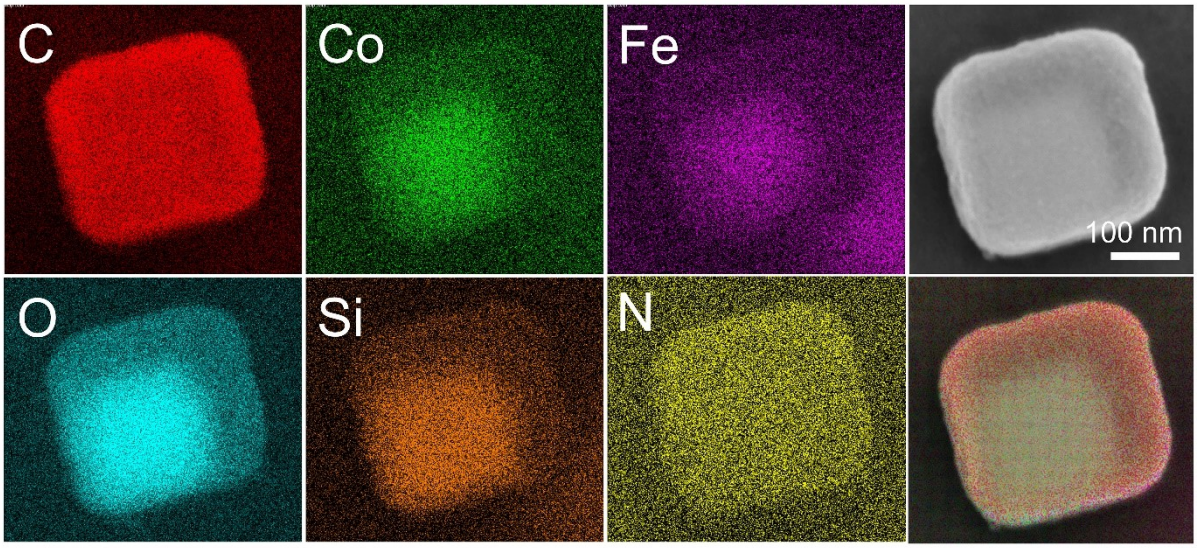

Fig. S8. EDS images of YS-FCF/GC@C.

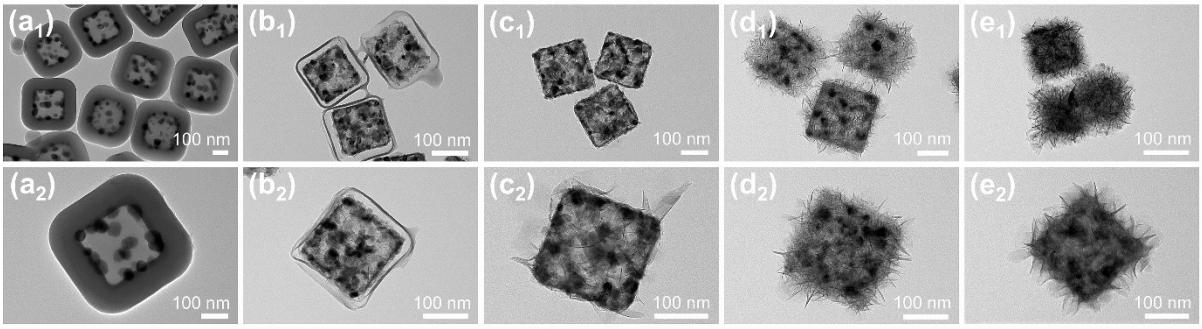

Fig. S9. TEM images (a_1-e_1) and magnified images (a_2-e_2) of the FCF/GC formation during the hydrothermal process.

The disappearance of SiO_2 was companied by the formation of lamellar GC. With the increase of hydrothermal time, the GC lamellae grew further spread out. In addition, restricted by the shape of the initial outer SiO_2 layers, FCF/GC cores eventually existed in the shape of cubes.

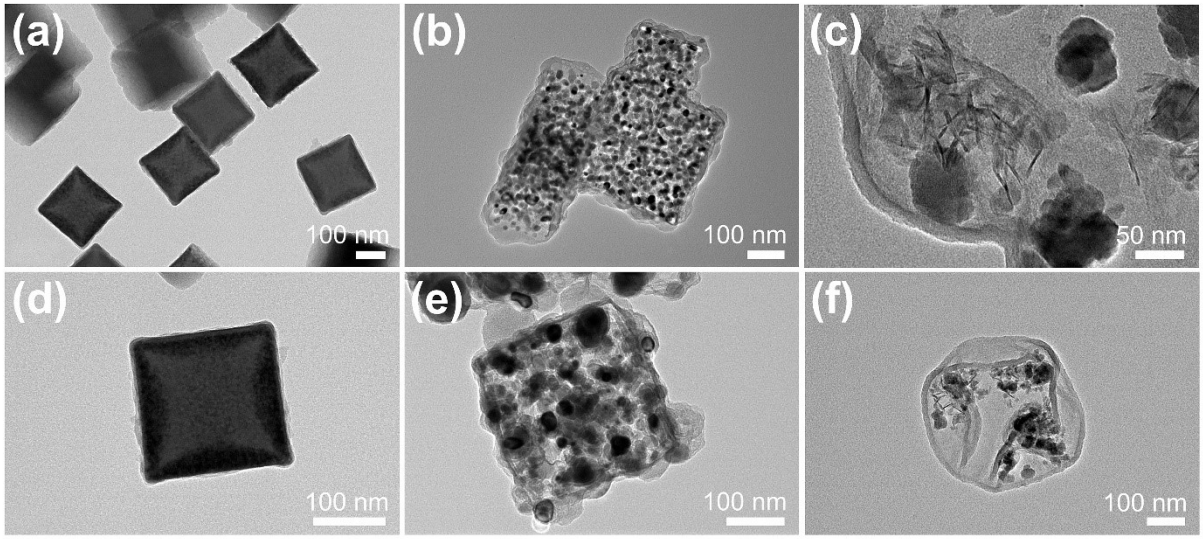

Fig. S10. TEM images of (a, d) FeCo PBA@PR, (b, e) FeCo/GC@C and (c, f) FCF/GC@C-1.

It could be noticed that lamellar GC did not participate in the formation of regular cubic cores without SiO_2, indicating that the slow etching process and shape restriction of SiO_2 were essential for the formation of cubic cores.

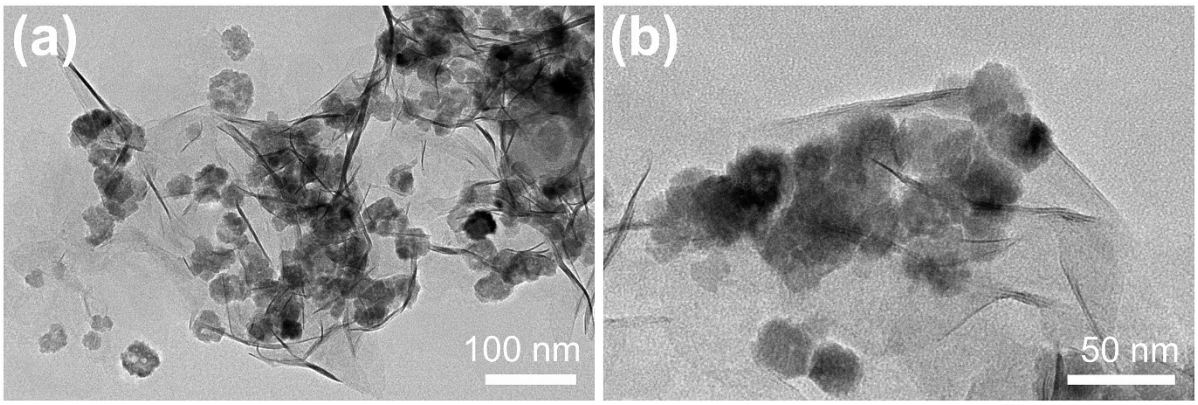

Fig. S11. TEM images of FCF and GC after hydrothermal etching in $NH_3 \cdot H_2O$ solution.

It is well-known that the depolymerization of SiO_2 will become more intense and rapid under alkaline conditions,[8] therefore, it could be observed that some of the nanoparticles and GC flowed out of the amorphous carbon shell in $NH_3 \cdot H_2O$ solution (1 mL $NH_3 \cdot H_2O$/ 80 mL DI water) and 2D GC was extremely thin and light, similar to that of graphene. Moreover, it could be demonstrated that 3D GC-based FCF/GC cores were made up of 2D GC lamellae and nanoparticles containing Fe, Co elements.

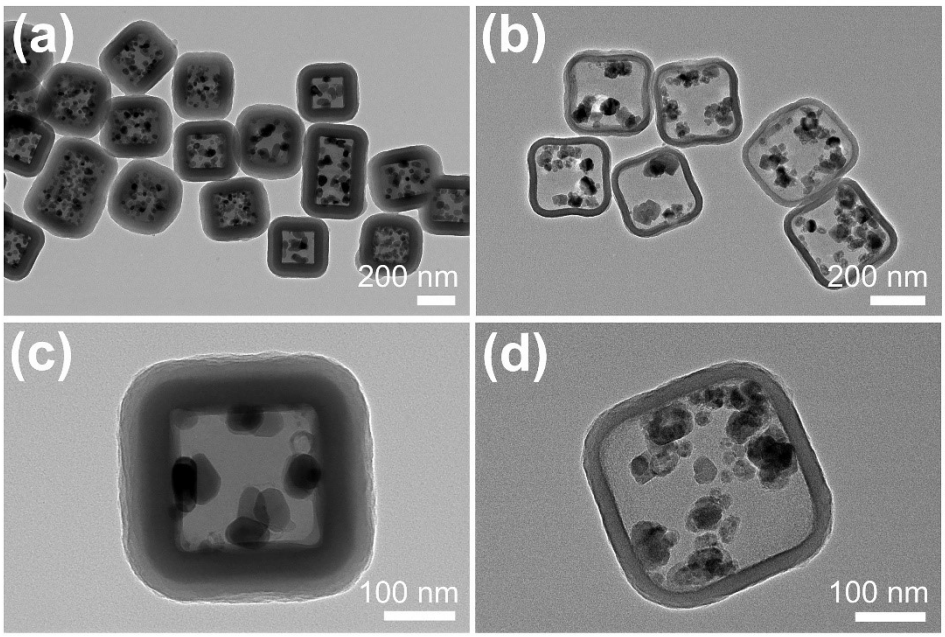

Fig. S12. TEM images of (a, c) FeCo/GC@SiO_2@C and (b, d) YS-FeCo/GC@C-KOH.

Etching of SiO_2 was also possible in KOH (60 ℃) solution. However, lamellar GC could not appear in an unsuitable etching environment, indicating that high temperature and pressure were required for the formation of lamellar GC. The EDS images of YS-FeCo/GC@C-KOH were shown in Fig. S13.

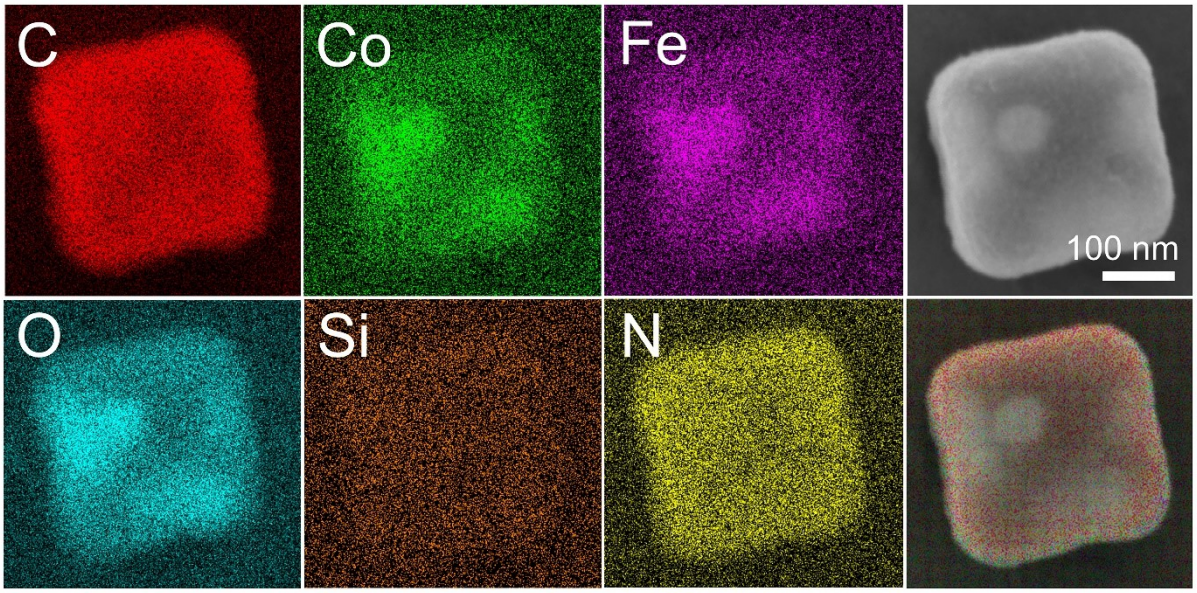

Fig. S13. EDS images of YS-FeCo/GC@C-KOH.

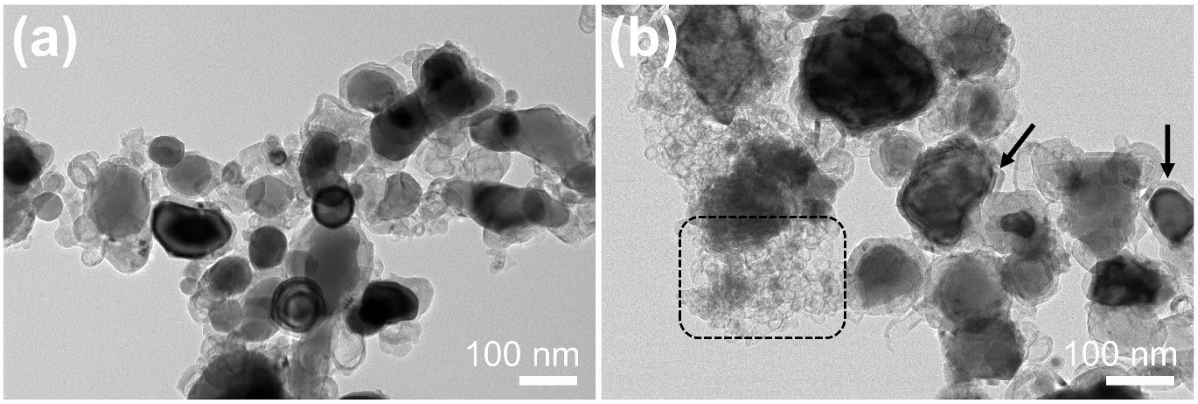

Fig. S14. TEM images of (a) FeCo/GC and (b) FCF/GC-1.

It can be observed that the combination of FeCo alloys with GC was not as tight as expected, and the disintegrations were noticeable after hydrothermal reaction (Fig. S14b), owing to the fact that GC was just simply catalyzed and unsteadily attached to FeCo alloys. However, without any coating, GC fragmented rather than transforming into lamellar GC. This fact underlined once again that the generation and expansion of lamellar GC could only be achieved under certain constraints.

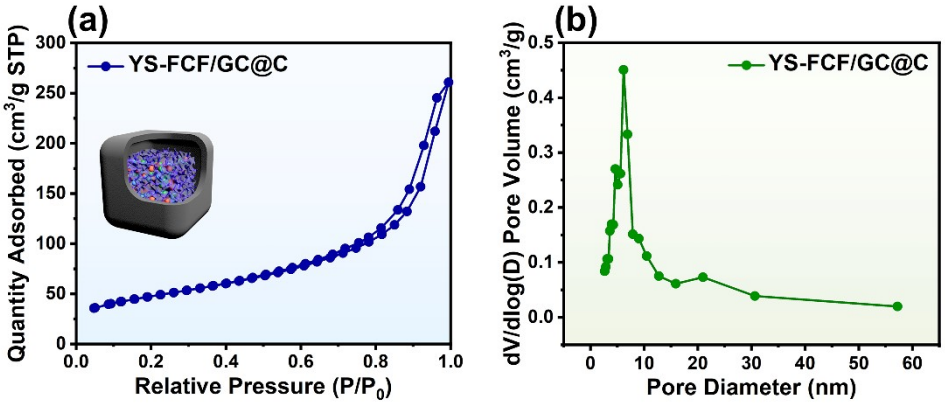

Fig. S15. N_2 adsorption-desorption isotherm and corresponding pore size distribution profile of YS-FCF/GC@C.

For YS-FCF/GC@C, there was a long and narrow hysteresis loop at a relative pressure (P/P_0) range of 0.75 to 1.0, which matched to the typical type IV isotherm, indicating the presence of mesoporous.[9-11] At the same time, the H3-type hysteresis loop showed that the presence of slit pores caused by the accumulation of sheet components in the measured composite (Fig. S15a).[12] The pore size distribution curve displayed a sharp and intense peak centered on ~6 nm (Fig. S15b), indicating that a significant number of nanoscale pores developed in the gaps of GC. Additionally, the specific surface area of YS-FCF/GC@C was up to 245.75 m^2 g^{-1}, which was beneficial to achieve large-scale interface polarization loss and reflection attenuation effect.[13]

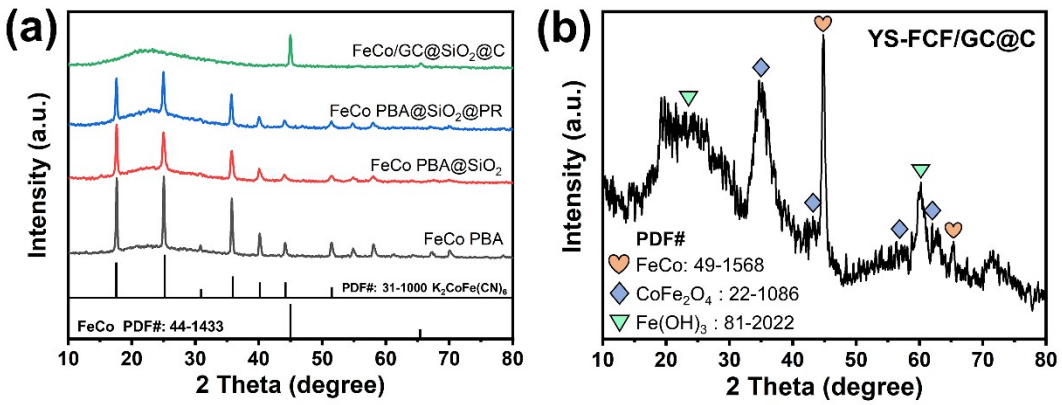

Fig. S16. XRD patterns of the samples obtained from multiple processes.

The phase behaviors were identified by XRD characterization. As shown in Fig. S16(a), the diffraction peaks at 17.6°, 24.9°, 30.9°, 35.6°, 10.0°, 44.1° and 51.3° corresponded well to the standard card of $K_2Co[Fe(CN)_6]$ (PDF# 31-1000), and the diffraction peaks at 44.8°and 65.3° were assigned to the (110) and (200) lattice planes of FeCo alloy (PDF# 49-1568), respectively.

In Fig. S16(b), the two characteristic peaks of FeCo located at 44.87° and 65.31°, corresponding to the (110) and (200) crystal planes, respectively. And the (311), (400), (511) and (440) crystal planes of $CoFe_2O_4$ (PDF# 22-1086) were confirmed through characteristic peaks of 35.44°, 43.06°, 56.97°and 62.59°. Besides, the diffraction peaks at 23.57° and 59.92° were ascribed to (002) and (242) crystal planes of $Fe(OH)_3$ (PDF# 81-2022).

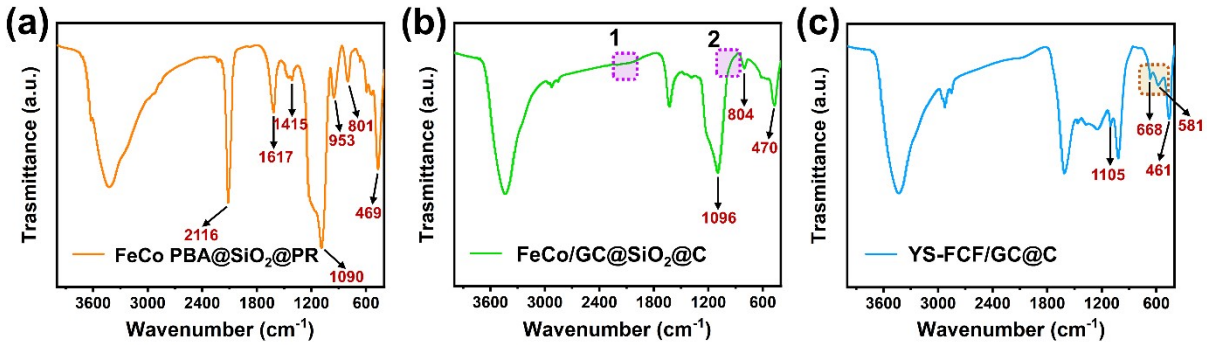

Fig. S17. FT-IR spectra of (a) FeCo PBA@SiO_2@PR, (b) FeCo/GC@SiO_2@C and (c) YS-FCF/GC@C.

The peaks at 1415 cm^{-1} and 1617 cm^{-1} were attributed to the aromatic C=C stretching vibration, indicating that the PR layer has been successfully coated. And the characteristic peaks at ~470 cm^{-1} represented the bending vibration of Si-O (Fig. S17a). In addition, because of the high-temperature dehydration condensation reaction of Si-OH, almost all of the Si-OH was transformed into Si-O-Si, and accordingly the bending vibration peak representing Si-OH at 953 cm^{-1} disappeared after carbonization. Similarly, the peak at 2116 cm^{-1} corresponding to -CN- bonds disappeared because the skeleton of FeCo PBA was difficult to maintain at high temperatures (Fig. S17b).

Two weak characteristic peaks located at 581cm^{-1} and 668cm^{-1} corresponding to Fe-O and Co-O bonds indicated the existence of a small amount of $CoFe_2O_4$ in YS-FCF/GC@C (Fig. S17c).[14] It was reported that the characteristic peak of Fe-O was at ~570 cm^{-1}, however, the absorption peak of Fe-O moving to a higher wave-number could be interpreted as particle size decreasing to the nano-scale.[15]

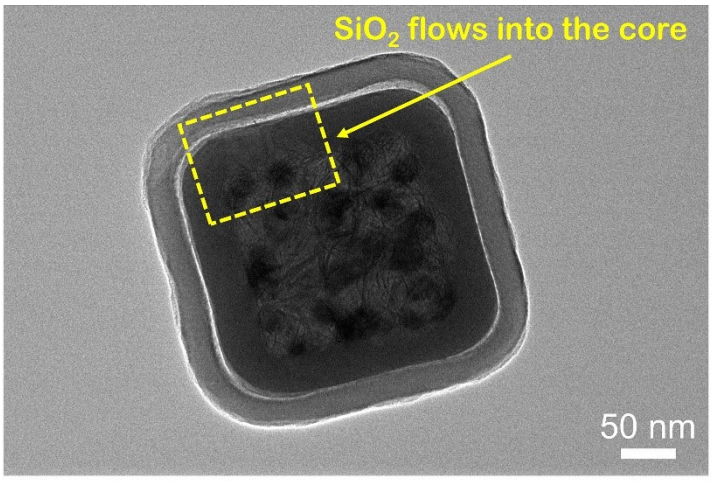

Fig. S18. TEM image of the transformation from FeCo/GC@SiO_2@C to YS-FCF/GC@C after 2 h hydrothermal reaction.

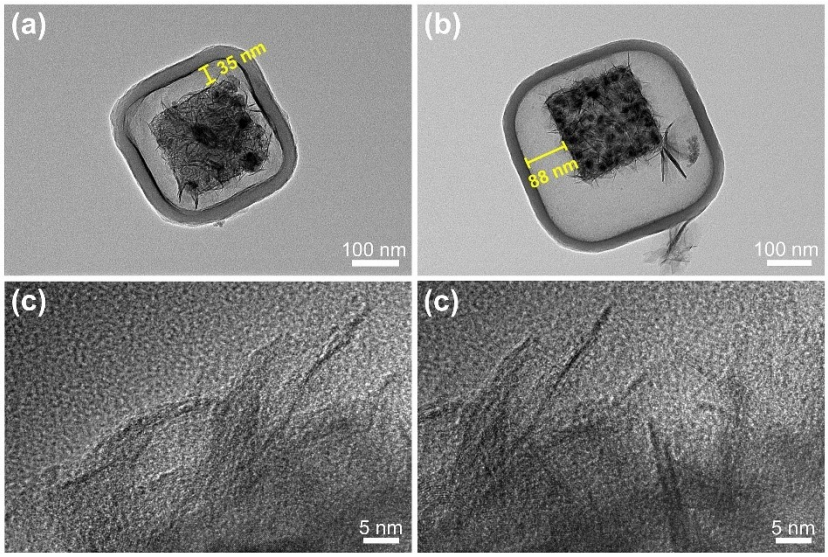

Fig. S19. TEM images of (a, b) YS-FCF/GC@C with different cavity sizes and HRTEM images of (c, d) corresponding GC in FCF/GC cores.

The TEM images indicated that either a thinner SiO_2 layer (~35 nm) or a thicker SiO_2 layer (~88 nm) had no effect on the ultimate morphology, and GC still underwent a morphology transformation process during a 15 h hydrothermal reaction.

What's more, as the thickness of the SiO_2 layer decreased, the FCF/GC core formed during the hydrothermal process became "looser", demonstrating the morphology-supporting effect of SiO_2. However, once the amount of SiO_2 flowing into the FCF/GC core reaches a certain degree, that is, saturation, the excess SiO_2 will disappear during the depolymerization reaction, leaving the FCF/GC core unaltered in terms of "compaction degree".

At the same time, it was worth noting that when the SiO_2 layer thickness increased, the outside PR layer became thinner. Also, when the thickness of the SiO_2 layer decreased, the outer PR layer's thickness increased correspondingly. This was because the amount of resorcinol and formaldehyde used in the PR coating process remained consistent. When the overall surface area of the FeCo PBA@SiO_2 nanocubes was increased, the same quantity of PR would exist at a thinner thickness, resulting in a thinner carbon layer following carbonization. The corresponding relationship was SiO_2 (~35 nm) --- C (~35 nm), SiO_2 (~50 nm) --- C (~27 nm) and SiO_2 (~ 88 nm) --- C (~ 23 nm).

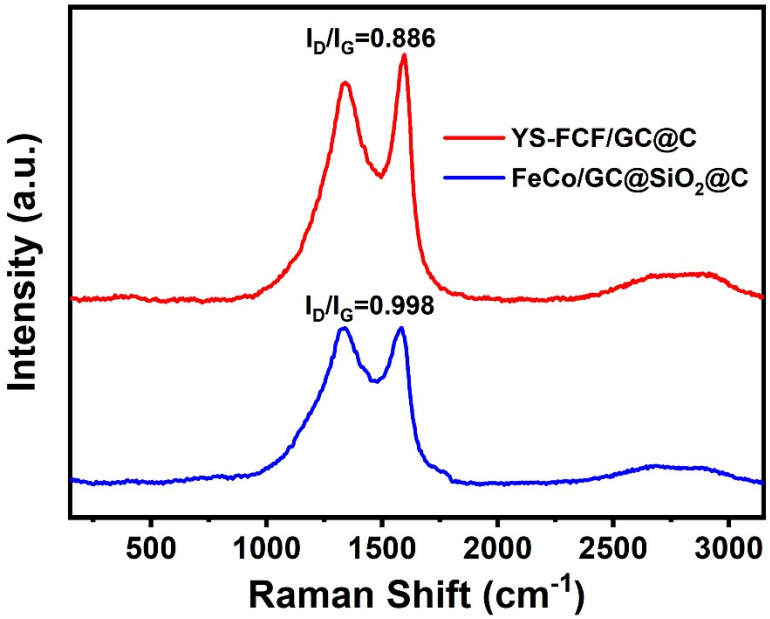

Fig. S20. Raman spectra of FeCo/GC@SiO_2@C and YS-FCF/GC@C.

It has been well-documented that the D-band is related to disordered or finite-sized crystals of graphite, while the G-band is derived from both graphite and all sp^2 sites. The three-stage model proposed by Ferrari and Robertson demonstrated the relationship between graphitization and I_D/I_G.[16] And the second stage is the transition from amorphous carbon to nanocrystalline graphite, with the relative intensity of the D peak continuously increasing.

During the high-temperature carbonization, metals catalyzed amorphous carbon around them, and the graphitization degree of the micro-area increased. However, along with the morphological transformation during hydrothermal process, the graphitization degree of micro-area decreased due to different existence forms of graphite species and local fragmentation of graphite microcrystallites.

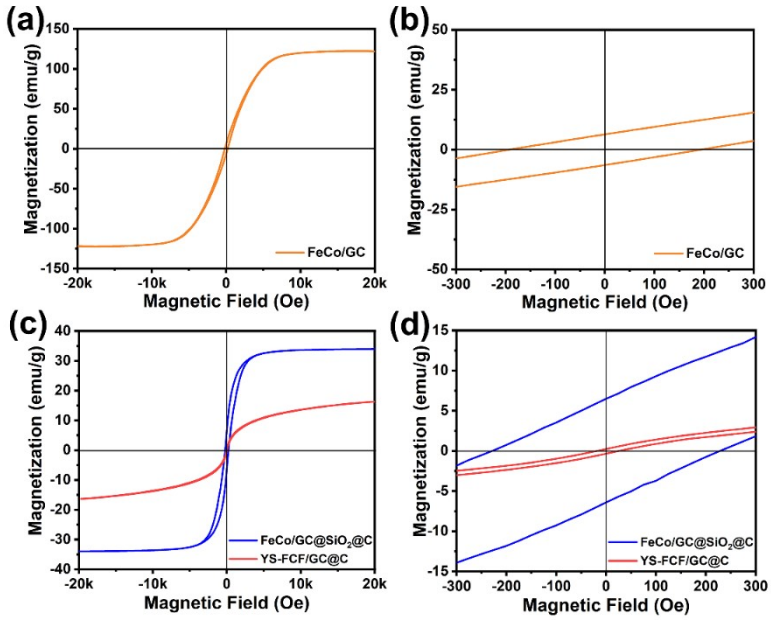

Fig. S21. (a, c) Hysteresis loops and (b, d) partial magnified details of FeCo/GC, FeCo/GC@SiO_2@C and YS-FCF/GC@C.

The saturation magnetization (M_s) values of FeCo/GC@SiO_2@C and YS-FCF/GC@C were 34.12 emu g^{-1} and 16.30 emu g^{-1}, respectively. These two values were found to be significantly lower than that of FeCo/GC of 121.93 emu g^{-1}. For SiO_2 and amorphous carbon, both of which are non-magnetic components, would diminish the magnetic response of FeCo/GC@SiO_2@C under an applied magnetic field. And after hydrothermal etching, the M_s value of YS-FCF/GC@C was further reduced because of the transformation of magnetic components. Magnified images revealed that FeCo/GC and FeCo/GC@SiO_2@C samples were ferromagnetic, while the YS-FCF/GC@C sample did not exhibit an evident ferromagnetic characteristic but behaved similar to a quasi-superparamagnetic behaviour due to its relatively low remanent magnetization and coercive force (H_c) value.[16] In fact, the degree of spontaneous magnetization of ferromagnetic materials decreases with the increase of temperature, as thermal motion seriously destroys the flat orientation of the spin magnetic moment of electrons. When the temperature reaches a certain level, a portion of the magnetic moment cancels each other out, resulting in a decrease in magnetic properties.

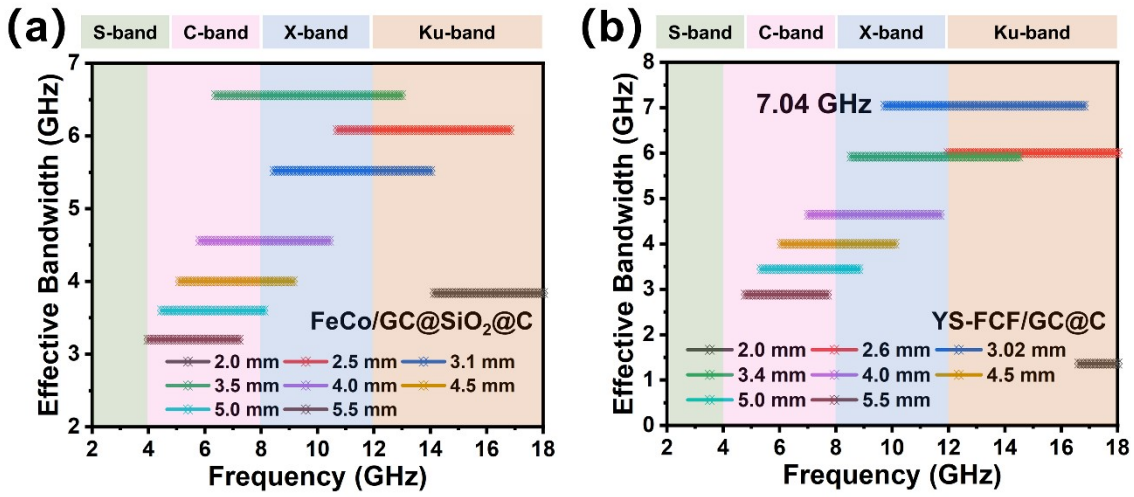

Fig. S22. EAB and RL values of (a) FeCo/GC@SiO_2@C and (b) YS-FCF/GC@C corresponding to different fitting thicknesses ranging from 2.0 to 5.5 mm.

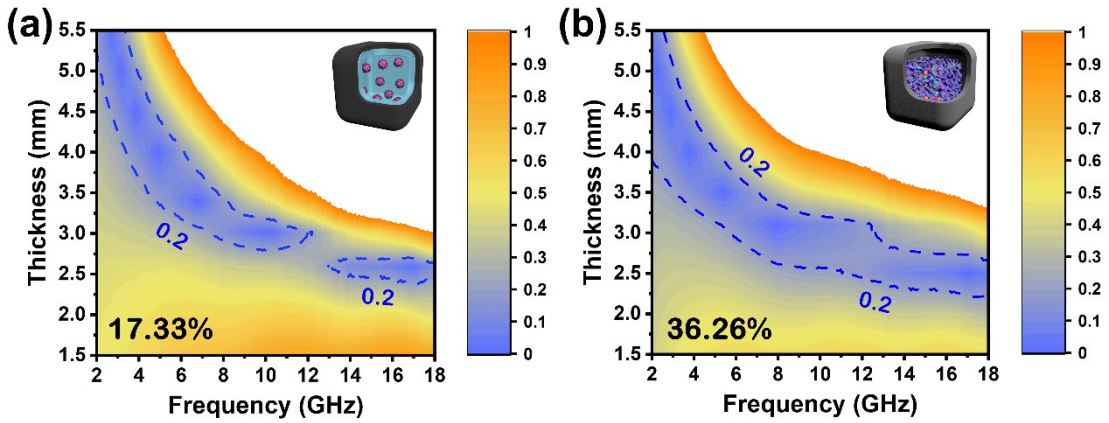

Fig. S23. Calculated delta value maps of (a) FeCo/GC@SiO_2@C and (b) YS-FCF/GC@C

A so-called delta-function has been developed to evaluate the degree of impedance matching, and it can be calculated using the following equation, [17-19]

$$|\Delta| = |sinh^2(Kfd) - M| \tag{2}$$

, where K and M are determined by ε' and μ' as

$$K = \frac{4\pi\sqrt{\mu'\varepsilon'}\cdot sin(\frac{\delta_e + \delta_m}{2})}{c\cdot cos\delta_e \cdot cos\delta_m} \tag{3}$$

$$M = \frac{4\mu' cos\delta_e \cdot \varepsilon' cos\delta_m}{(\mu' cos\delta_e - \varepsilon' cos\delta_m)^2 + [tan(\frac{\delta_m}{2} - \frac{\delta_e}{2})]^2 \cdot (\mu' cos\delta_e + \varepsilon' cos\delta_m)^2} \tag{4}$$

.

It is widely accepted that a small delta value, particularly for $|\triangle| < 0.2$, indicates good impedance matching (RL< -8 dB).[20] The integral coverages with desired delta values of FeCo/GC@SiO_2@C and YS-FCF/GC@C were 17.33% and 36.26%, respectively, showing that a better impedance matching has been realized in YS-FCF/GC@C.

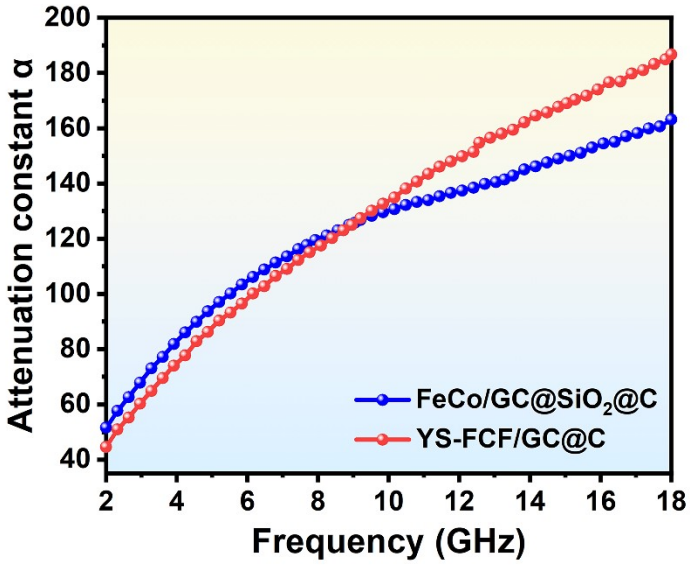

Fig. S24. Attenuation coefficients α of FeCo/GC@SiO_2@C and YS-FCF/GC@C.

Table S1. Position and assignment of FT-IR peaks.

ν (CN) cm^{-1}	ν (CN) cm^{-1}	ν (NH) cm^{-1}
Fe^{II}-C≡N-Co^{II}	Fe^{II}-C≡N-Co^{III}	NH^{4+}
2099	2158	1411

Table S2. Morphologies under different hydrothermal times in the transformation from FeCo@GC@SiO_2@C to YS-FCF/GC@C (corresponding to Fig. 3).

State	a_1	b_1	c_1	d_1
Time	0 h	2.5 h	4 h	5.5 h
State	e_1	f_1	g_1	h_1
Time	7 h	9.5 h	11 h	15 h

Table S3. Reflection loss characteristics of various magnetic carbon-based composites and this work.

Sample	Loading ratio (wt%)	Thickness (mm)	RL (dB)[a)]	EAB (GHz)[b)]	Refs.
Ni@C@ZnO	25	2.5	-55.8	4.1	21
ZnO/$ZnFe_2O_4$/C@PG	25	2.7	-54.6	5.36	12
Honeycomb-like Co/C	10	2.9	-50.7	4.6	22
FeCo/NPC-2.0	50	1.2	-21.7	5.8	23
NC@Co/NC	25	2.2	-52.5	4.4	24
Rod-like Co/C	22	2.0	-47.6	5.11	25
CoZn/C	40	2.5	-45.2	5.7	26
Air@NC/Ni-Co	25	2.2	-36.5	6.55	27
CoO/Co@C	70	1.5	-38.46	4.8	28
Co/MnO@C	25	2.4	-55.3	4.6	29
NiO/Ni/C@C@Air@ NiO/Ni/C	50	1.7	-34.5	~5.5	30
ZnO/C@Co/C	50	1.9	-28.8	4.2	31
CoMo@NC	30	2.5	-44.8	6.56	32
CN-2.5	20	1.6	-53	5.08	33
Co/C-700	25	3.0	-30.31	4.93	34
YS-FCF/GC@C	**40**	**3.02**	**-60.03**	**7.04**	**This Work**

[a)] Minimum value of reflection loss; [b)] Effective absorption bandwidth

Table S4. Reflection loss characteristics of various yolk-shell composites and this work.

Sample	Loading ratio (wt%)	Thickness (mm)	RL (dB)[a)]	EAB (GHz)[b)]	Refs.
C@C	50	1.85	-39.4	5.4	35
H-Fe_3O_4@C	30	1.9	-58.44	6.0	36
ZnO@600C	60	2.0	-50.05	5.68	37
Fe@C	20	2.5	-45.53	4.3	38
n-Ni_xS_y@NSC-800	30	1.5	-37.2	3.84	39
$ZnFe_2O_4$@PHCMS	/	4.8	-51.43	3.52	40
YS-ZFO@RGO@TiO_2	33.3	2.6	-44.3	4.1	41
1D flower-like yolk-shell FSN nanochains	30	2.54	-54.28	4.0	42
C-ZIF-67@TiO_2	50	1.65	-51.7	~4.25	43
Fe_3O_4@C	40	3.0	-45.8	5.6	44
Co_3Fe_7@C	65	2.0	-35.3	~6.0	45
Fe_3O_4@C	60	1.5	-45.4	~3.8	46
Fe_3O_4/PANI	50	5.0	-46.0	~5	47
YS-FCF/GC@C	**40**	**3.02**	**-60.03**	**7.04**	**This Work**

[a)] Minimum value of reflection loss; [b)] Effective absorption bandwidth

Supplementary References

1 Z. X. Cai, Z. L. Wang, J. Kim and Y. Yamauchi, *Adv. Mater.*, 2019, **31**, 1804903.
2 Y. Feng, X. Y. Yu and U. Paik, *Chem Commun*, 2016, **52**, 6269-6272.
3 A. Kumar and S. Bhattacharyya, *ACS Appl. Mater. Interfaces*, 2017, **9**, 41906-41915.
4 J. Nai, Y. Lu, L. Yu, X. Wang and X. W. D. Lou, *Adv. Mater.*, 2017, **29**, 1703870.
5 J. Liao, J. Qiu, G. Wang, R. Du, N. Tsidaeva and W. Wang, *J. Colloid Interface Sci.*, 2021, **604**, 537-549.
6 Y. Feng, X. Y. Yu and U. Paik, *Sci. Rep.*, 2016, **6**, 34004.
7 Y. Lu, X. Zhang, X. Mao and Y. Huang, *J. Mater. Chem. B*, 2019, **7**, 4661-4668.
8 Q. Liu, Q. Cao, H. Bi, C. Liang, K. Yuan, W. She, Y. Yang and R. Che, *Adv. Mater.*, 2016, **28**, 486-490.
9 X. Xu, F. Ran, Z. Fan, Z. Cheng, T. Lv, L. Shao and Y. Liu, *ACS Appl. Mater. Interfaces*, 2020, **12**, 17870-17880.
10 J. Yan, Y. Huang, Y. Yan, L. Ding and P. Liu, *ACS Appl. Mater. Interfaces*, 2019, **11**, 40781-40792.
11 L. Wang, X. Jiao, P. Liu, Y. Ouyang, X. Xia, W. Lei and Q. Hao, *Appl.Surf.Sci.*,2018, **427**, 174-181.
12 S. Song, A. Zhang, L. Chen, Q. Jia, C. Zhou, J. Liu and X. Wang, *Carbon*, 2021, **176**, 279-289.
13 J. Liang, J. Chen, H. Shen, K. Hu, B. Zhao and J. Kong, *Chem. Mater.*, 2021, **33**, 1789-1798.
14 X. F. Lu, L. F. Gu, J. W. Wang, J. X. Wu, P. Q. Liao and G. R. Li, *Adv Mater*, 2017, **29**, 1604437.
15 G. Zhao, J.-J. Feng, Q.-L. Zhang, S.-P. Li and H.-Y. Chen, *Chem. Mater.*, 2005, **17**, 3154-3159.
16 Y. Du, W. Liu, R. Qiang, Y. Wang, X. Han, J. Ma and P. Xu, *ACS Appl. Mater. Interfaces*, 2014, **6**, 12997-13006.
17 Y. Wang, X. Han, P. Xu, D. Liu, L. Cui, H. Zhao and Y. Du, *Chem. Eng. J.*, 2019, **372**, 312-320.
18 N. Yang, Z. X. Luo, S. C. Chen, G. Wu and Y. Z. Wang, *ACS Appl. Mater. Interfaces*, 2020, **12**, 18952-18963.
19 H. Zhang, Z. Jia, A. Feng, Z. Zhou, L. Chen, C. Zhang, X. Liu and G. Wu, *Composites, Part B*, 2020, **199**, 108261.
20 Z. Ma, C.-T. Cao, Q.-F. Liu and J.-B. Wang, *Chin. Phys. Lett.*, 2012, **29**, 038401.
21 L. Wang, X. Yu, X. Li, J. Zhang, M. Wang and R. Che, *Chem. Eng. J.*, 2020, **383**, 123099.
22 L. Wang, X. Bai, B. Wen, Z. Du and Y. Lin, *Composites, Part B*, 2019, **166**, 464-471.
23 X. Zhang, G. Ji, W. Liu, B. Quan, X. Liang, C. Shang, Y. Cheng and Y. Du, *Nanoscale*, 2015, **7**, 12932-12942.
24 P. Liu, S. Gao, Y. Wang, Y. Huang, W. He, W. Huang and J. Luo, *Chem. Eng. J.*, 2020, 381, 122653.
25 J. Li, P. Miao, K.-J. Chen, J.-w. Cao, J. Liang, Y. Tang and J. Kong, *Composites, Part B*, 2020, **182**, 107613.
26 J. Pan, W. Xia, X. Sun, T. Wang, J. Li, L. Sheng and J. He, *Appl. Surf. Sci.*, 2020, 512,

144894.
27 H. Qiu, X. Zhu, P. Chen, J. Liu and X. Zhu, *Compos. Commun.*, 2020, **20**, 100354.
28 X. Wang, P. Zhou, G. Qiu, X. Zhang, L. Wang, Q. Zhang, M. Wang and Z. Liu, *J. Alloys Compd.*, 2020, **842**, 155807.
29 D. Xu, N. Wu, K. Le, F. Wang, Z. Wang, L. Wu, W. Liu, A. Ouyang and J. Liu, *J. Mater. Chem. C*, 2020, **8**, 2451-2459.
30 X. Liang, B. Quan, Y. Sun, G. Ji, Y. Zhang, J. Ma, D. Li, B. Zhang and Y. Du, *Part. Part. Syst. Charact.*, 2017, **34**, 1700006.
31 X. Liang, B. Quan, G. Ji, W. Liu, Y. Cheng, B. Zhang and Y. Du, *Inorg. Chem. Front.*, 2016, **3**, 1516-1526.
32 W. Huang, X. Zhang, Y. Zhao, J. Zhang and P. Liu, *Carbon*, 2020, **167**, 19-30.
33 Y. Cheng, H. Zhao, H. Lv, T. Shi, G. Ji and Y. Hou, *Adv. Electron. Mater.*, 2019, **6**, 1900796.
34 H. Wang, L. Xiang, W. Wei, J. An, J. He, C. Gong and Y. Hou, *ACS Appl. Mater. Interfaces*, 2017, **9**, 42102-42110.
35 R. Qiang, Y. Du, Y. Wang, N. Wang, C. Tian, J. Ma, P. Xu and X. Han, *Carbon*, 2016, **98**, 599-606.
36 W. Ma, P. He, T. Wang, J. Xu, X. Liu, Q. Zhuang, Z.-K. Cui and S. Lin, *Chem. Eng. J.*, 2021, **420**, 129875.
37 L. Yan, M. Zhang, S. Zhao, T. Sun, B. Zhang, M. Cao and Y. Qin, *Chem. Eng. J.*, 2020, **382**, 122860.
38 W. Chu, K. Wang, H. Li, Y. Chen and H. Liu, *Chem. Eng. J.*, 2022, **430**, 133112.
39 B. Li, M. Liu, W. Zhong, J. Xu, X. Zhang, X. Zhang, X. Zhang and Y. Chen, *Carbon*, 2021, **182**, 276-286.
40 L. Chai, Y. Wang, N. Zhou, Y. Du, X. Zeng, S. Zhou, Q. He and G. Wu, *J. Colloid Interface Sci.*, 2021, **581**, 475-484.
41 J. Feng, Y. Wang, Y. Hou and L. Li, *Inorg. Chem. Front.*, 2017, **4**, 935-945.
42 M. Ma, W. Li, Z. Tong, W. Huang, R. Wang, P. Lyu, Y. Ma, G. Wu, Q. Yan, P. Li and X. Yao, *J. Alloys Compd.*, 2020, **843**, 155199.
43 X. Zhang, G. Ji, W. Liu, X. Zhang, Q. Gao, Y. Li and Y. Du, *J. Mater. Chem. C*, 2016, **4**, 1860-1870.
44 K. Wang, G. Wan, G. Wang, Z. He, S. Shi, L. Wu and G. Wang, *J. Colloid Interface Sci.*, 2018, **511**, 307-317.
45 H. Li, S. Bao, Y. Li, Y. Huang, J. Chen, H. Zhao, Z. Jiang, Q. Kuang and Z. Xie, *ACS Appl. Mater. Interfaces*, 2018, **10**, 28839-28849.
46 S. Gao, Y. Zhang, H. Xing and H. Li, *Chem. Eng. J.*, 2020, **387**, 124149.
47 X. Wang, M. Zhang, J. Zhao, G. Huang and H. Sun, *Appl. Surf. Sci.*, 2018, **427**, 1054-1063.